High Performance Nano-Crystalline Oxide Fuel Cell Materials: Defects, Structures, Interfaces, Transport, and Electrochemistry

S.A. Barnett, L.D. Marks, T.O. Mason, K. Poeppelmeier, P.W. Voorhees
Northwestern University
September 7, 2016

Abstract

This project addresses fundamental materials challenges in solid oxide electrochemical cells, devices that have a broad range of important energy applications. Although nano-scale mixed ionically and electronically conducting (MIEC) materials provide an important opportunity to improve performance and reduce device operating temperature, durability issues threaten to limit their utility and have remained largely unexplored. Our work has focused on both (1) understanding the fundamental processes related to oxygen transport and surface-vapor reactions in nano-scale MIEC materials, and (2) determining and understanding the key factors that control their long-term stability. Furthermore, materials stability has been explored under the "extreme" conditions encountered in many solid oxide cell applications, *i.e*, very high or very low effective oxygen pressures, and high current density.

Technical Achievements

Oxygen Electrode Stability

Morphological stability of nano-scale electrode materials and prediction of long-term performance based on accelerated testing. *We believe that these results will lead to a new paradigm in the search for improved MIEC materials – one that includes not only anion (oxygen) transport but also the cation transport factors that determine stability.* New processing methods such as atomic layer deposition have been developed and are being explored to produce to more stable nano-electrode microstructures. Determination of the critical electrolysis current densities (overpotentials) where oxygen electrode degradation begins, *significant for development of materials whose properties can be tuned to yield optimal performance and stability;*

$(Sr_{0.5}Sm_{0.5})CoO_{3-\delta}$ (SSC) is one of the highest performance fast oxygen transport MIEC materials – in prior work, we studied these properties in detail, and also produced nano-scale SSC oxygen electrodes with polarization resistance R_P amongst the lowest ever reported at target operating temperatures (~600^{o}C). We have now also carried out detailed electrochemical impedance spectroscopy studies that help elucidate the correlation between processing, electrode structure, materials' transport properties, and performance. Here the results on materials stability are highlighted.

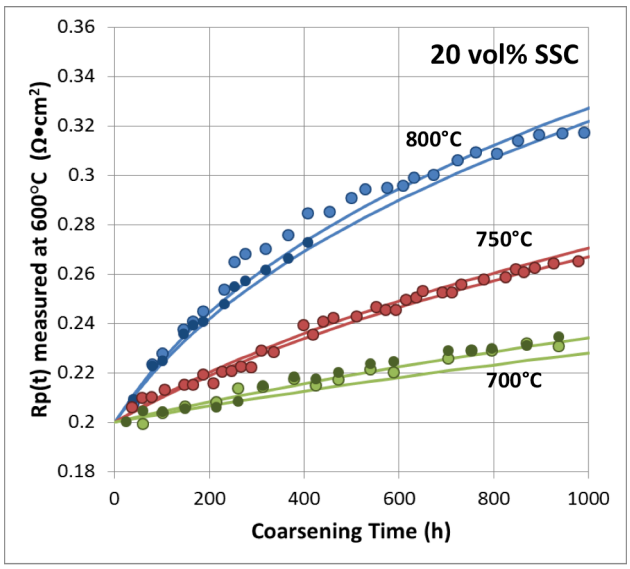

Figure 1. R_P measured at 600°C in air, versus time for $(Sm_{0.5}Sr_{0.5})Co_3$ nano-scale electrodes at various elevated temperature designed to accelerate degradation. Power-law coarsening fits are also shown.

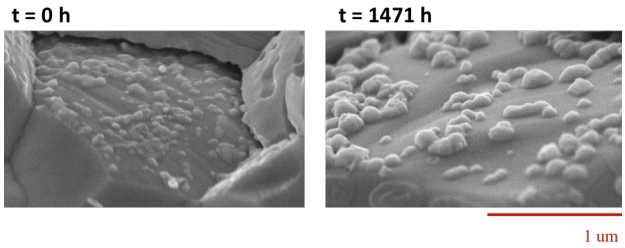

Figure 2. Scanning electron microscope images of nano-scale SSC on a Gd-doped Ceria (GDC) scaffold, before annealing and after 1471 h at 800°C.

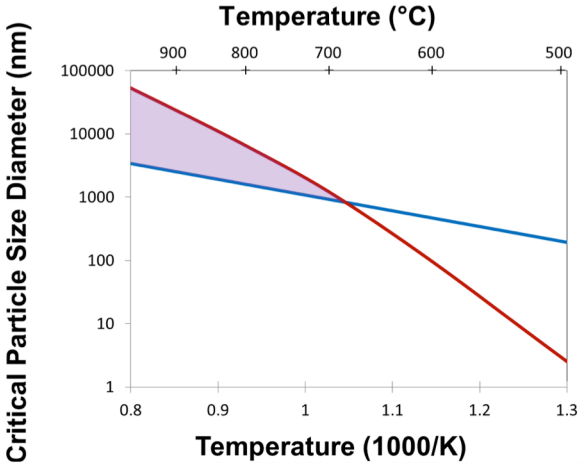

Figure 3. Critical particle size versus temperature. The blue line indicates the size above which the degradation rate over 40,000 h is < 0.2%/kh. The red line gives the size below which RP is acceptable, < 0.2 Ω cm2. The shaded indicates the particle size and temperature range where a stable low-RP electrode is achieved.

The long-term stability of highly active nano-scale cathodes, such as SSC, has not previously been studied and remains a potential show-stopper (solid state ionic devices such as fuel cells that should operate at temperature for > 40,000 h). Figure 1 summarizes results from accelerated tests, showing more rapid R_P degradation with time at higher temperature. Figure 2 shows images indicating that a key change in the electrode after annealing is coarsening of SSC nano-particles. The results in Figure 1 were thus fitted using a model that accounts for power-law particle coarsening and its effect on R_P:

$$R_p = \left(Bexp(-E_D/kT_c)t + R_{p0}^n\right)^{1/n} \quad (1)$$

where t is time, $R_{P,0}$ is initial resistance, T_c is temperature, E_D is a diffusion activation energy, B includes a diffusion coefficient pre-factor and electrochemical terms, and n is the power law. After fitting the data with n = 4, corresponding to a surface diffusion process, eq. 1 is used to predict degradation rates for different particle sizes and temperatures. The results are summarized in Figure 3, which also shows the size below which R_P is suitably low. Unfortunately, the shaded region, indicating the particle size and temperature range where a stable low- R_P electrode is achieved, extends only down to ~ 700°C and ~ 1000 nm particle size! (Note, however, that a very stringent stability criterion was used here – relaxing this to 0.5%/kh, or 25% R_P increase over 40,000 h, extends this down to nearly 600°C and 100 nm.) There are two important implications of these results: (1) experimental work needs to focus on methods to improve stability, and (2) theoretical work, which to date has focused entirely on optimizing oxygen transport kinetics,[1,2] must also consider stability, *i.e.,* the cation diffusion processes that controls particle coarsening.

With these results in mind, initial experiments have been done to explore whether stability can be improved by altering the electrode morphologically. Initial experiments were carried out where a thin layer of a relatively stable material, ZrO_2, was deposited onto the SSC nano-particles using atomic layer deposition. The results in Figure 4 show that the coating yields an improvement in initial R_P as well as a reduced degradation rate, in basic agreement with an initial report on coated nano-electrodes.[3]

It is also important to understand the effects of cell operating conditions on stability – electrical potentials and currents yield high fields and large local swings in effective oxygen partial pressure, in many cases directly impacting materials stability and properties.[4,5] Figure 5 provides an example of LSCF electrodes where increasing the current density, and hence the electrode overpotential, increases degradation. The results suggest that degradation occurs when the overpotential exceeds ~ 300 mV, corresponding to any oxygen pressure > 1000 bar. Substantial changes in electrode microstructure are observed due to the high effective pressure.

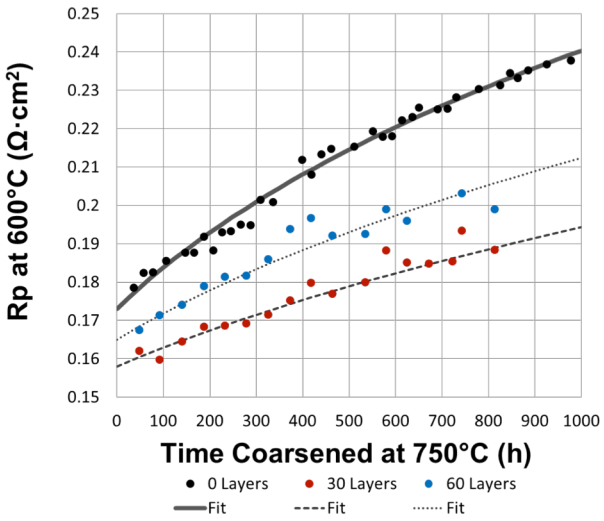

Figure 4. R_P versus time at 750°C for a conventional electrode and one coated with 5 nm (red) and 10 nm thick (blue) ZrO_2 layers by atomic layer deposition.

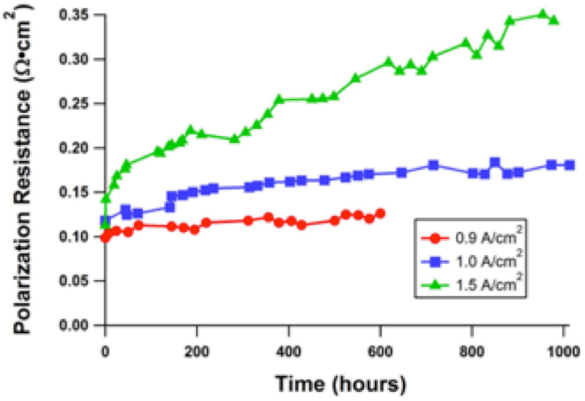

Figure 5. R_P versus time of an LSCF electrode during reversing-current life tests at current density values of 0.9, 1.0, and 1.5 A/cm².

Oxygen Reduction Mechanisms

Determination of oxygen reduction mechanisms on MIEC nano-scale electrodes has been achieved using electrochemical impedance spectroscopy.

Oxygen reduction kinetic parameters – oxygen ion diffusion D_δ and surface exchange coefficient k – were determined for porous $Nd_2NiO_{4+\delta}$ solid oxide cell electrodes as a function of temperature and oxygen partial pressure by analyzing

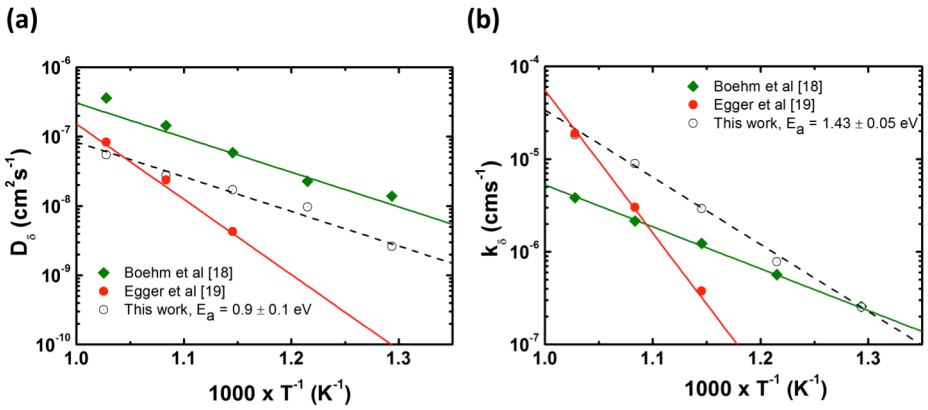

Figure 6. Comparison between D (a) and k (b) obtained in this work and those reported previously.

electrochemical impedance spectroscopy data using the Adler-Lane-Steele model.[6] Three-dimensional electrode microstructural data were used in model. Figure 6 illustrates the measured transport coefficients obtained compared with prior measurements on bulk materials.

Figure 7 shows varying $La_{1-x}Sr_xCr_{1-x}Fe_xO_{3-\delta}$ (LSCrFe) fuel electrode compositions that were found to exhibit decreased R_P with increasing Fe and Sr content (x), which correlated with increase oxygen deficiency δ. For the conditions tested here – humidified hydrogen – LSCrFe with x = 0.4-0.7 yielded good performance and phase stability. However, in fuel cells and electrolysis cells the oxygen pressure may vary from ~ 10^{-14} to 10^{-30} bar – in this case, varying x in LSCrFe will provide a means to "tune" stability and properties (via oxygen deficiency) to best match a given operating condition.

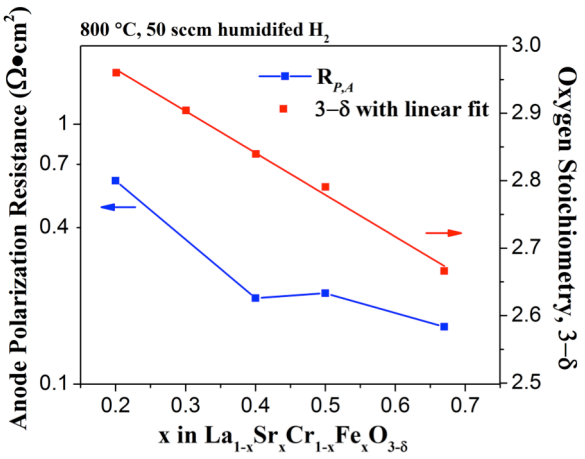

Figure 7. R_P and oxygen stoichiometry 3-δ versus composition x for $La_{1-x}Sr_xCr_{1-x}Fe_xO_{3-\delta}$ measured at 800°C in humidified H_2 fuel.

High Performance Cathode Materials

Oxygen tracer diffusion (D*) and chemical diffusion ($\tilde{D}$) were measured in dense $Sr_{0.5}Sm_{0.5}CoO_{3-\delta}$ (SSC) ceramics by Isotope Exchange Depth Profiling/Secondary Ion Mass Spectrometry and electrical conductivity relaxation. As shown in Figure 8, SSC exhibits higher oxygen chemical diffusivity than other reported solid oxide cell cathodes. Oxygen surface exchange rates have also been measured (not shown) and are amongst the best among known materials.

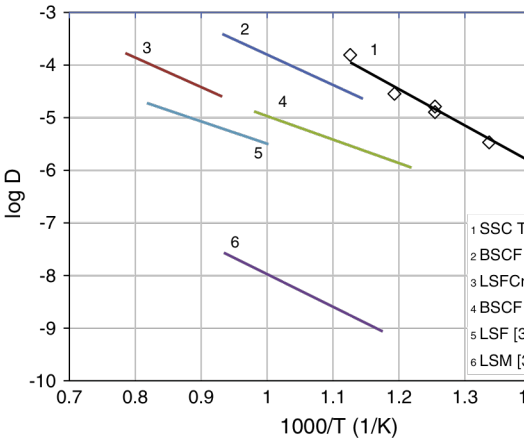

Figure 8. Chemical diffusivities of the SSC material (data points) compared with literature values for other high performance SOC air-electrode materials.

This same high performance material has been explored in nano-scale electrodes, producing amongst the lowest reported air-electrode polarization resistances. Detailed impedance spectroscopy studies were carried out in collaboration with University of Karlsruhe, Germany, to explore the electrochemical processes in SSC electrodes with nano-scale structure. Dependences on P_{O2} and T provide signatures of specific physical processes, separated by fitting the impedance spectra. Figure 9 shows an example of the variation of a cathode's impedance spectrum with P_{O2}, where three main processes can be identified that varied with P_{O2}: (1) the low frequency (~ 10 Hz) resistance varies as P_{O2}^{-1} which, together with very weak temperature dependence, indicates gas diffusion, but is only important at very low P_{O2}; (2) the dominant mid-frequency (10^3 – 10^4 Hz) response varies much more weakly with P_{O2}, but strongly with temperature, a signature that it represents a combination of oxygen surface exchange and oxygen ion diffusion; (3) the high frequency resistance (>10^5 Hz, on the shoulder of the mid frequency peak) does not vary with P_{O2}, but does vary with temperature, and so may be related to charge transfer across interfaces, possibly between SSC and the Gd-doped Ceria electrolyte. Overall, these results show that it is mainly the surface exchange and oxygen ion diffusion processes that limit the cathode performance; these results are being compared with the above fundamental measurements of these processes using microstructure-dependent cathode models.

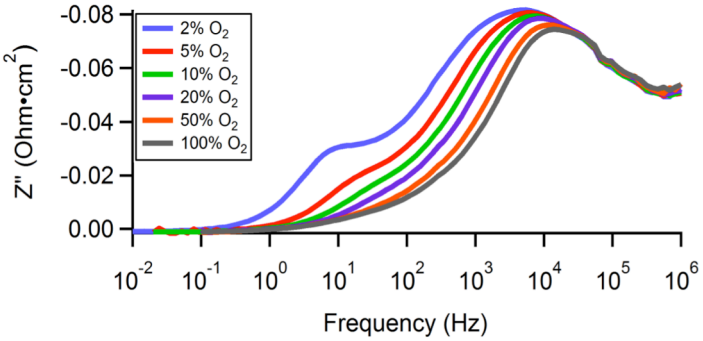

Figure 9. Impedance spectra from an infiltrated SSC cathode on Gd-doped Ceria, measured at various oxygen partial pressures at 600°C.

Fundamentals of Infiltrated Nano-Electrodes

Infiltration of one material into a scaffold, such as the SSC infiltration into GDC mentioned above, is an important avenue for achieving good low-temperature electrode performance. The infiltrate size scale and interconnectivity, which have a major effect on the polarization resistance, are related to the size and location of the liquid droplets that are present on the scaffold surface following the evaporation of the liquid. However, there has been no way of predicting this process. We have developed a model that predicts the size of these droplets. Their size scale, ~50 nm (Figure 10) is reasonably consistent with experiments. The model is not limited to a planar surface, and thus can be used to assess the development of the infiltrated phase upon subsequent loadings.

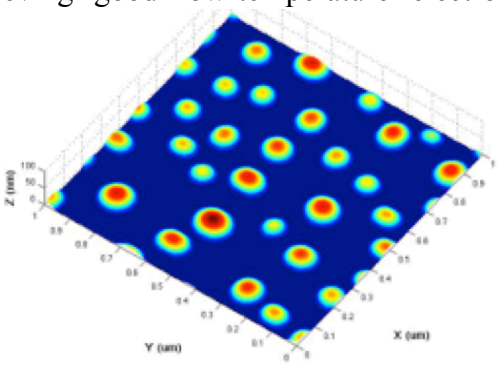

Figure 10. A simulation of the liquid film evaporation process, showing the formation of liquid droplets on a surface.

Oxide Anode Electrochemistry

A picture of the electrochemical rate-limiting steps of perovskite-oxide anodes is beginning to emerge based on detailed impedance spectroscopy studies. Figure 11 illustrates an example of impedance data from a cell with a $(La_{0.33}Sr_{0.67})(Fe_{0.67}Cr_{0.33})O_3$ anode under varying H_2 partial pressures P_{H2} (balance Ar with 3% H_2O). The Bode plot shows a main electrochemical process with a peak frequency at 2 Hz that varies strongly with P_{H2}. (The process at ~1000 Hz is mainly due to the cathode.) While a low-frequency response with a strong P_{H2} dependence is often associated with gas diffusion, this is not the case here because the response is strongly temperature dependent. On the other hand, such a response, along with the limiting-current behavior seen in current-voltage characteristics, can be explained well by a H_2 dissociative adsorption rate-limiting process.

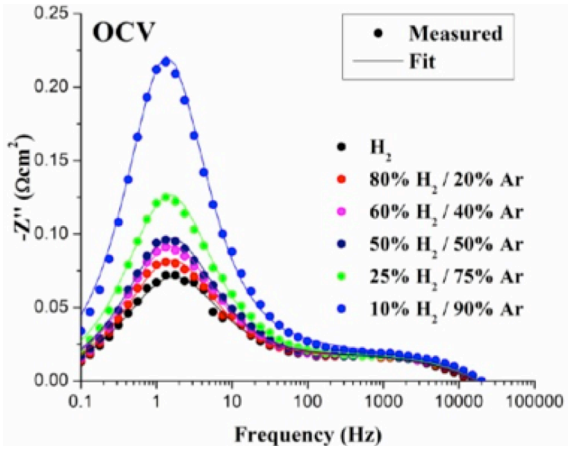

Figure 11. Bode plots of impedance spectra measured from a SOFC at 800°C at open circuit voltage with different H_2 partial pressures. Fits are also shown.

We have developed an expression for this H_2 adsorption rate-limiting process based on the work of Mench[7] which we have fit to R_{LF} versus P_{H2} data for various oxide anodes:

$$R_P = \left(\frac{d\eta}{dj}\right)_{j=0} = \frac{RT}{zFj_0^{\theta=1}}\left[\frac{k_{1f}P_{H2} + k_{1b}}{k_{1f}P_{H2}}\right] \quad (2)$$

where η is the overpotential, j is the current, R is the gas constant, z is the charge associated with the reaction, F is Faraday's constant, $j_0^{\theta=1}$ is the exchange current density at the maximum hydrogen surface coverage, k_{1f} is the hydrogen adsorption rate coefficient, k_{1b} is the hydrogen desorption rate coefficient. A best fit of this equation to data obtained for a $LaSr_2Fe_2CrO_{9-\delta}$-GDC anode cell tested under various P_{H2} values is shown in Figure 12. This model demonstrates a reasonable agreement with the data (R^2 = 0.97355) and accounts for the strong temperature dependence observed for these anodes.

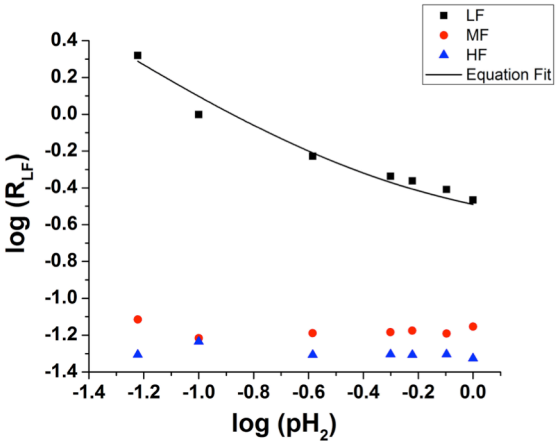

Figure 12. Low (LF), medium (MF), and high (HF) frequency resistances of a $LaSr_2Fe_2CrO_{9-\delta}$-GDC anode cell at 800°C versus H_2 partial pressure obtained from fits to the EIS data. A fit of the LF data to Equation 2 is also shown.

These H_2 adsorption limitation expressions also imply a limiting-current behavior in current-voltage characteristics. We have also developed an expression attributing this behavior to adsorptive and desorptive losses:

$$V = V_0 - jR_\Omega - \frac{RT}{\alpha zF}sinh^{-1}\frac{jRT}{2\alpha zFR_{pol,cat}} - \frac{RT}{\alpha zF}sinh^{-1}\frac{jzFN_s\left(k_{1b}+k_{1f}P_{H_2}\right)}{j_0^{\theta=1}\left(zFk_{1f}P_{H_2}N_s - j\right)} \quad (3)$$

where V_0 is the open-circuit voltage, R_Ω is the Ohmic resistance, α is the transfer coefficient associated with the reaction, $R_{pol,cat}$ is the polarization resistance due to the cathode, N_s is the total number of sites occupied by adsorbed H atoms. Best fits of Equation 3 to current-voltage data at various P_{H2} for a $La_{0.33}Sr_{0.67}Fe_{0.67}Cr_{0.33}O_{3-\delta}$-GDC anode cell are shown in Figure 13. Again, the model agrees well with the data. Current and future work is aiming to refine this equation to remove low P_{H2} deviations by breaking down the hydrogen oxidation process into multiple steps rather than relying on a one-step dissociative adsorption process. The influence that temperature and P_{H2} have on the limiting mechanism is also being explored by incorporating charge transfer processes into more recent model iterations. Regardless, we have observed that promotion of H_2 dissociative adsorption is important to improve performance in oxide anode cells. Our future work aims to determine how changing anode properties such as chemical composition, microstructure, and catalytic substituents can further promote H_2 dissociative adsorption.

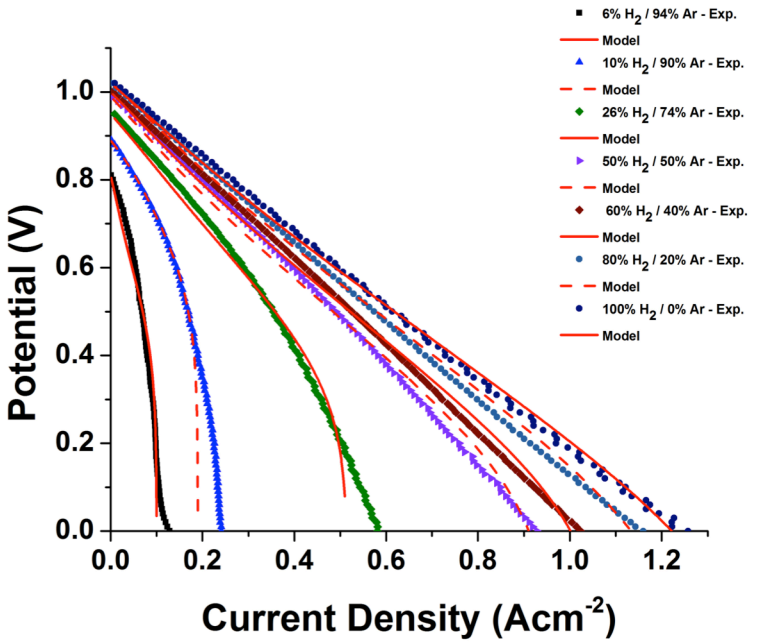

Figure 13. Equation 2 fits to $La_{0.33}Sr_{0.67}Fe_{0.67}Cr_{0.33}O_{3-\delta}$-GDC anode cell current-voltage data under various P_{H2}.

Anode Nanoparticle Effects

We have further explored novel oxide anode materials where catalytic nano-particles nucleate during SOC operation. Figure 14 shows a TEM image of a $(La_{0.8}Sr_{0.2})(Fe_{0.5}Cr_{0.3}Ru_{0.2})O_3$ particle that was exposed to hydrogen at elevated temperature resulting in self-assembly of surface Ru nano-particles that greatly improve anode performance. The image shown is just one of a rotation series being reconstructed to produce a 3D image – such imaging will allow us quantify particle nucleation and growth and thereby understand their role in electrochemical processes.

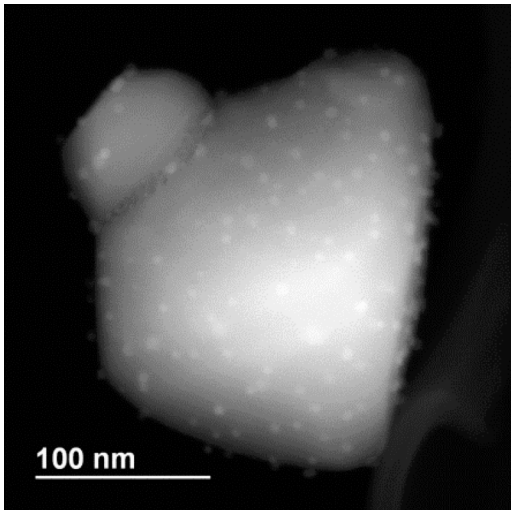

Figure 14. Z-contrast TEM image of a $(La,Sr)(Fe,Cr,Ru)O_3$ particle decorated with Ru nano-particles.

Figure 15 shows that when Ru is added to the perovskite oxide anode such that Ru nanoparticles form, the anode polarization resistance is reduced. The resistance generally decreases with increasing Ru content. Note that the dependence on P_{H2} also becomes weaker when Ru is added to the oxide, a clear indicator of a change in mechanism. Finally, the limiting-current behavior in current-voltage curves disappears. These are all indications that Ru nanoparticle formation eliminates H_2 adsorption as a rate-limiting step, with hydrogen electrochemical

oxidation becoming the new rate-limiting step. The Ru nanoparticles presumably act as catalysts for H_2 dissociation with subsequent spillover of H atoms onto the adjacent oxide surface, where the oxidation process is thereby enhanced.

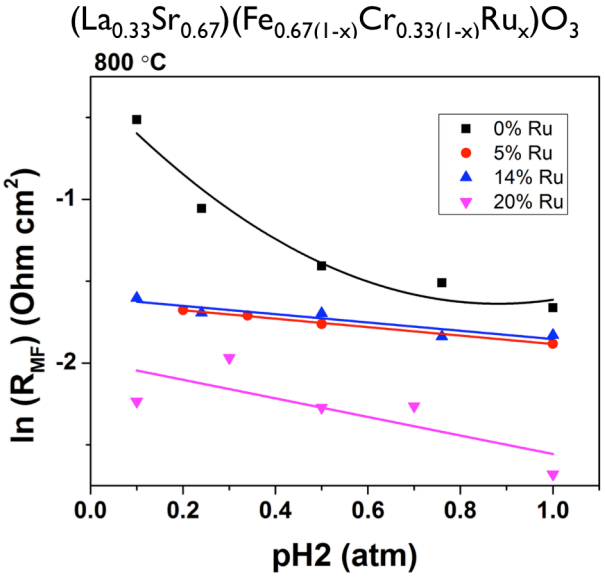

Figure 15. Polarization resistance versus P_{H2} for chromite anodes with varying Ru amounts.

Our study of the materials properties of Pd-substituted (La,Sr)$CrO_{3-\delta}$ (LSCrPd) anodes has continued to uncover new insights into the actual phase in which catalytically active Pd metal is present. While we have previously shown LSCrPd to be a robust redox-stable anode material due to the regenerable exsolution of Pd metal[8], more recent structural studies using high resolution powder x-ray diffraction at the Advanced Photon Source at Argonne National Laboratories have put into question the actual nature of and degree to which substitution of Pd into the perovskite lattice occurs. The powder X-ray diffraction (PXRD) patterns displayed in Figure 16 show, in addition to the majority (La,Sr)$CrO_{3-\delta}$ phase, other Pd-containing phases present in the materials, most notably La_4PdO_7. Using rapid acquisition temperature- and atmosphere-controlled PXRD, we were also able to determine that this non-perovskite secondary Pd-phase was regenerable upon redox cycle, adding further question to the actual source of the recoverable Pd in these anodes. Thus, in addition to continuing to study the phase behavior of the pure perovskite, future work using TEM and electrochemical cell testing will explore the activity of La_4PdO_7 in anode conditions.

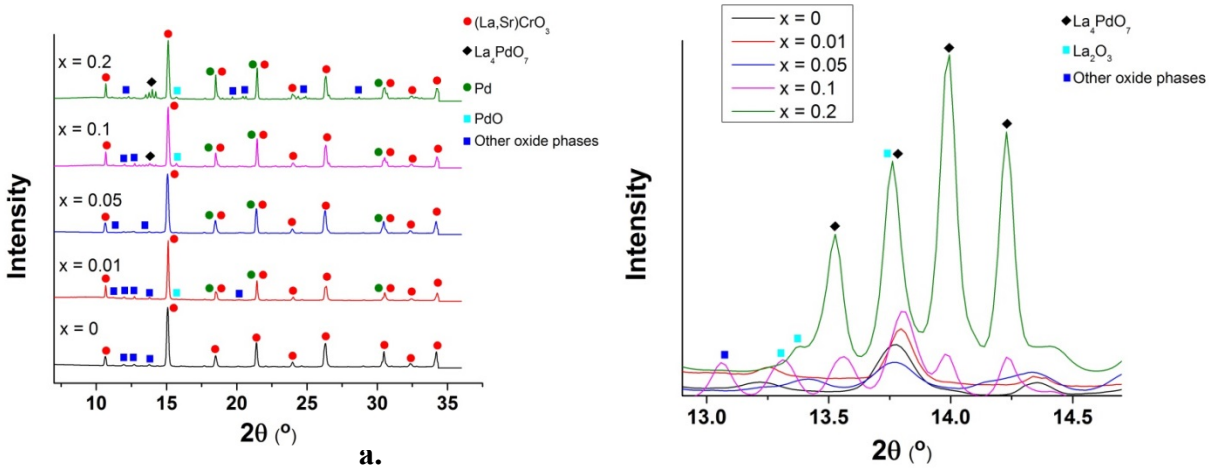

Figure 16: Powder X-ray diffraction patterns of Pd-substituted (La,Sr)CrO3-δ with different amounts of Pd substitution a.) (Left) from 10.0 to 35.0 2θ°, and b.) (Right) zoomed in to show reflections between 13.0 and 14.5 2θ°.

$LaO_{1.5}$-$GaO_{1.5}$-NiO Phase Diagram

$La_{1-x}Sr_xGa_{1-y}Mg_yO_{3-\delta}$ (LSGM) is a promising electrolyte material. However, issues with phase compatibility with common electrode materials, particularly Ni, have been reported. The thermodynamic stability of LSGM with nickel-containing electrode materials is being investigated by refining the $LaO_{1.5}$-$GaO_{1.5}$-NiO phase diagram at the processing temperature of 1400 °C. Particular interest lies in the compatibility of undoped $LaGaO_3$ with La_2NiO_4 and $La_4Ni_3O_{10}$ cathodes and NiO in anodes. Preliminary results suggest equilibrium between Ga-doped NiO and $LaGaO_3$ with low Ni content while equilibrium between $LaGaO_3$ and La_2NiO_4 is disrupted by the formation of Ga-doped $La_4Ni_3O_{10}$ and $La_4Ga_2O_9$. Investigations of equilibrium between Ga-doped $La_4Ni_3O_{10}$ and $LaGaO_3$ are ongoing.

Implementation in Intermediate Temperature Cells

An SOFC demonstration was made utilizing the new materials and structures developed in this project. A novel SOFC fabrication method, structure, and materials set was implemented to achieve arguably the best intermediate-temperature SOFC ever reported. The key to this result is the use of a nano-scale infiltrated SSC cathode based on our prior DoE work, along with the best currently available electrolyte (LSGM) and a nano-scale infiltrated Ni anode.

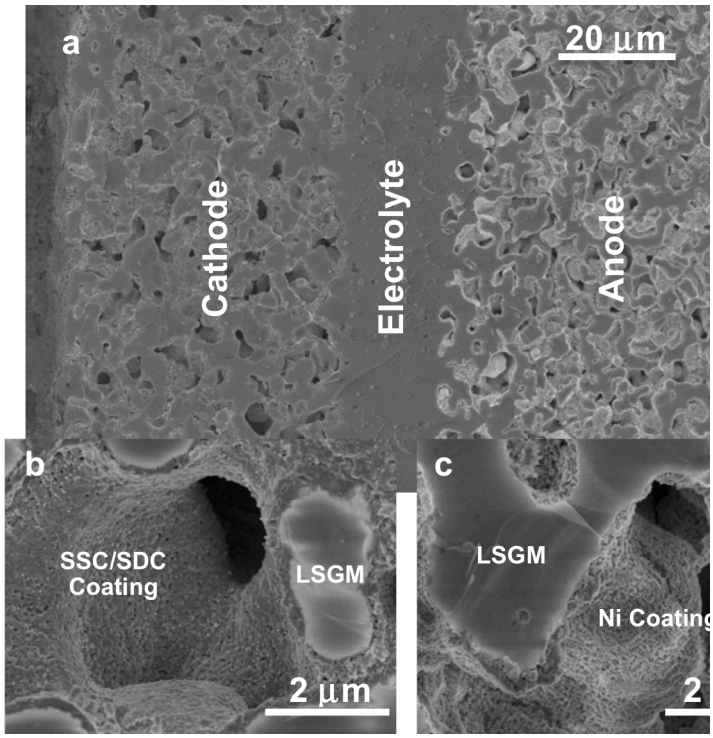

Figure 17. Cross-sectional scanning electron microscope (SEM) images showing an operated thin LSGM electrolyte cell. (a) A low magnification survey image. (b) A higher magnification view of the cathode. (c) A higher magnification view of the anode.

The cells were based on tri-layer porous/dense/porous LSGM structures, as shown in Figure 17a. This all-LSGM structure was fired at high temperature, with all subsequent processing steps being infiltration and low-temperature (≤850°C) calcination. This strategy avoids the materials interactions that plague LSGM, and also produces the nano-scale (high surface area) structure that promotes fast oxygen exchange at the cathode and fuel oxidation reactions at the anode. On the cathode side, the LSGM pore surfaces had a nano-porous coating of SSC (and in some cases $Sm_{0.2}Ce_{0.8}O_{1.9}$ (SDC)), as shown in Figure 17b. The anode side was coated with nano-porous Ni (Figure 17c). The average diameters of Ni and SSC particles were ≈ 50 nm.

Figure 18 shows cell voltages and power densities plotted versus current density, measured at temperatures of 450-600°C with humidifed hydrogen in the anode and ambient air in

the cathode. The open circuit voltage (OCV) values increased from 1.101 to 1.114 V with decreasing temperature, within 20 mV of the calculated Nernst potentials. This is critical because it shows the potential for high efficiency, and indicates that the processing yielded a ≈ 15 μm thick LSGM layer that was both gas tight and free of Ni impurities that can introduce electronic conductivity. The maximum power densities were 1.33, 1.06, 0.81 and 0.39 Wcm^{-2} at 600, 550, 500 and 450°C, respectively.

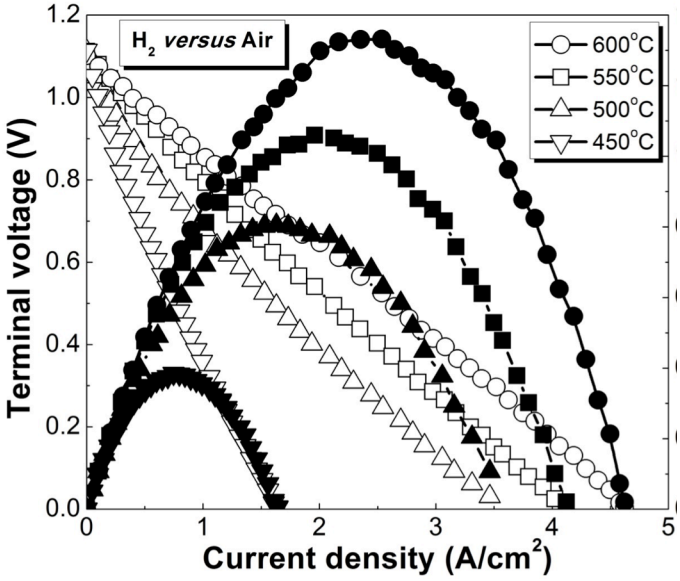

Figure 18. Performance plot in humidified hydrogen. Voltage and power density versus current density, measured in humidifed hydrogen fuel and ambient air at 450-600°C, from a thin LSGM electrolyte cell with electrode loadings V_{Ni} = 7.2% and $V_{SSC\text{-}SDC}$ = 12.9%.

At any given temperature, these values are world records; a few prior SOFCs yielded power densities nearly as good, but only with relatively low open circuit voltage (OCV) values that render them impractical for most applications. Although there are prior reports of pulsed laser deposited LSGM-electrolyte cells that produced as high power density at 600°C (but lower than the present values at < 600°C), they had low OCV values, apparently because they required a bi-layer LSGM/SDC electrolyte[9,10]. Similarly, doped-Ceria electrolyte cells have produced power densities approximately half of the present values, but only with low OCV. Thus, the fundamental materials research in this project has led to a technological breakthrough in fuel cells.

References

1 Lee, Y.-L., Kleis, J., Rossmeisl, J., Shao-Horn, Y. & Morgan, D. Prediction of solid oxide fuel cell cathode activity with first-principles descriptors. *Energy & Environmental Science* **4**, 3966, doi:10.1039/c1ee02032c (2011).

2 Wang, L., Merkle, R., Mastrikov, Y. A., Kotomin, E. A. & Maier, J. Oxygen exchange kinetics on solid oxide fuel cell cathode materials—general trends and their mechanistic interpretation. *Journal of Materials Research* **27**, 2000-2008, doi:10.1557/jmr.2012.186 (2012).

3 Gong, Y. H., Palacio, D., Song, X. Y., Patel, R. L., Liang, X. H., Zhao, X., Goodenough, J. B. & Huang, K. Stabilizing Nanostructured Solid Oxide Fuel Cell Cathode with Atomic Layer Deposition. *Nano Letters* **13**, 4340-4345, doi:Doi 10.1021/Nl402138w (2013).

4 Chen, M., Liu, Y. L., Bentzen, J. J., Zhang, W., Sun, X., Hauch, A., Tao, Y., Bowen, J. R. & Hendriksen, P. V. Microstructural Degradation of Ni/YSZ Electrodes in Solid Oxide Electrolysis Cells under High Current. *Journal of the Electrochemical Society* **160**, F883-F891, doi:10.1149/2.098308jes (2013).

5 Knibbe, R., Traulsen, M. L., Hauch, A., Ebbesen, S. D. & Mogensen, M. Solid Oxide Electrolysis Cells: Degradation at High Current Densities. *Journal of The Electrochemical Society* **157**, B1209-B1217, doi:Doi 10.1149/1.3447752 (2010).

6 Lu, Y., Kreller, C. & Adler, S. B. Measurement and Modeling of the Impedance Characteristics of Porous La[sub 1−x]Sr[sub x]CoO[sub 3−δ] Electrodes. *Journal of The Electrochemical Society* **156**, B513, doi:10.1149/1.3079337 (2009).

7 Mench, M. M. *Fuel Cell Engines*. 157 (Wiley, 2008).

8 Bierschenk, D. M., Potter-Nelson, E., Hoel, C., Liao, Y., Marks, L., Poeppelmeier, K. R. & Barnett, S. A. Pd-substituted (La,Sr)CrO3−δ–Ce0.9Gd0.1O2−δ solid oxide fuel cell anodes exhibiting regenerative behavior. *Journal of Power Sources* **196**, 3089-3094, doi:10.1016/j.jpowsour.2010.12.050 (2011).

9 Yan, J., Matsumoto, H., Akbay, T., Yamada, T. & Ishihara, T. Preparation of LaGaO3-based perovskite oxide film by a pulsed-laser ablation method and application as a solid oxide fuel cell electrolyte. *Journal of Power Sources* **157**, 714-719 (2006).

10 Yan, J. W., Matsumoto, H., Enoki, M. & Ishihara, T. High-power SOFC using La0.9Sr0.1Ga0.8Mg0.2O3-delta/Ce0.8Sm0.2O2-delta composite film. *Electrochem Solid St* **8**, A389-A391, doi:Doi 10.1149/1.1943568 (2005).

Publications From This DoE Grant

1. Zhu, T., Fowler, D. E., Poeppelmeier, K. R., Han, M. & Barnett, S. A. Hydrogen Oxidation Mechanisms on Perovskite Solid Oxide Fuel Cell Anodes. *Journal of The Electrochemical Society* **163**, F952-F961, doi:10.1149/2.1321608jes (2016). *Full DoE support.*
2. Duffy, P. K., Barnett, S. A. & Mason, T. O. A Hemispherical Electrolyte Probe for Screening of Solid Oxide Fuel Cell Cathode Materials. *Journal of The Electrochemical Society* **163**, F802-F807, doi:10.1149/2.0341608jes (2016). *Full DoE Support*
3. Wang, H., Yakal-Kremski, K. J., Yeh, T., Rupp, G. M., Limbeck, A., Fleig, J. & Barnett, S. A. Mechanisms of Performance Degradation of (La,Sr)(Co,Fe)O3-δSolid Oxide Fuel Cell Cathodes. *Journal of The Electrochemical Society* **163**, F581-F585, doi:10.1149/2.0031607jes (2016). *Main support by DoE.*
4. Kennouche, D., Chen-Wiegart, Y.-c. K., Yakal-Kremski, K. J., Wang, J., Gibbs, J. W., Voorhees, P. W. & Barnett, S. A. Observing the microstructural evolution of Ni-Yttria-stabilized zirconia solid oxide fuel cell anodes. *Acta Materialia* **103**, 204-210, doi:10.1016/j.actamat.2015.09.055 (2016). *Partial support by DoE.*
5. Call, A. V., Railsback, J. G., Wang, H. & Barnett, S. A. Degradation of nano-scale cathodes: a new paradigm for selecting low-temperature solid oxide cell materials. *Physical chemistry chemical physics : PCCP* **18**, 13216-13222, doi:10.1039/c6cp02590k (2016). *Main support by DoE.*
6. Gao, Z., Mogni, L. V., Miller, E. C., Railsback, J. G. & Barnett, S. A Perspective On Low-Temperature Solid Oxide Fuel Cells. *Energy & Environmental Science*, doi:10.1039/C5EE03858H (2016). *Main support by DoE.*
7. Gao, Z., Zenou, V., Kennouche, D., Marks, L. D. & Barnett, S. Characteristics of Solid Oxide Cells with Zirconia/Ceria Bi-Layer Electrolytes Fabricated Utilizing Reduced-Temperature Firing. *J. Mater. Chem. A*, doi:10.1039/c5ta01964h (2015). *Partial support by DoE.*
8. Fowler, D. E., Messner, A. C., Miller, E. C., Slone, B. W., Barnett, S. A. & Poeppelmeier, K. R. Decreasing the Polarization Resistance of (La,Sr)CrO3−δSolid Oxide Fuel Cell Anodes by Combined Fe and Ru Substitution. *Chem Mater*, 150514130523002, doi:10.1021/acs.chemmater.5b00622 (2015). *Full DoE Support*
9. Hughes, G. A., Railsback, J. G., Yakal-Kremski, K. J., Butts, D. M. & Barnett, S. A. Degradation of (LaSr)MnO-ZrYO composite electrodes during reversing current operation. *Faraday Discuss*, doi:10.1039/c5fd00020c (2015). *Partial support by DoE.*
10. Railsback, J. G., Gao, Z. & Barnett, S. A. Oxygen electrode characteristics of Pr2NiO4+δ-infiltrated porous (La0.9Sr0.1)(Ga0.8Mg0.2)O3–δ. *Solid State Ionics* **274**, 134-139, doi:10.1016/j.ssi.2015.03.030 (2015). *Full DoE Support*
11. Yakal-Kremski, K., Mogni, L. V., Montenegro-Hernandez, A., Caneiro, A. & Barnett, S. A. Determination of Electrode Oxygen Transport Kinetics Using Electrochemical Impedance Spectroscopy Combined with Three-Dimensional Microstructure Measurement: Application to Nd2NiO4+delta. *Journal of the Electrochemical Society* **161**, F1366-F1374, doi:Doi 10.1149/2.0521414jes (2014). *Full DoE Support*
12. Fowler, D. E., Haag, J., Boland, C., Bierschenk, D. M., Barnett, S. A. & Poeppelmeier, K. R. Stable, Low Polarization Resistance Solid Oxide Fuel Cell Anodes: La1-xSrxCr1-

xFexO3-δ(x=0.2-0.67) *Chem Mater*, 140428025107009, doi:10.1021/cm500423n (2014). *Main support by DoE.*

13. Miller, E. C., Gao, Z. & Barnett, S. A. Fabrication of Solid Oxide Fuel Cells with a Thin (La0.9Sr0.1)0.98(Ga0.8Mg0.2)O3-δElectrolyte on a Sr0.8La0.2TiO3Support. *Fuel Cells* **13**, 1060-1067, doi:10.1002/fuce.201300155 (2013). *Partial support by this grant*
14. Cho, S., Fowler, D. E., Miller, E. C., Cronin, J. S., Poeppelmeier, K. R. & Barnett, S. A. Fe-substituted SrTiO3−δ–Ce0.9Gd0.1O2 composite anodes for solid oxide fuel cells. *Energy & Environmental Science*, doi:10.1039/c3ee23791e (2013). *Partial support by this grant*
15. Z. Zhan, D. Han, T. Wu, X. Ye, S. Wang, T. Wen, S. Cho and S.A. Barnett, "A solid oxide cell yielding high power density below 600 °C," *RSC Advances* **2** (2012) 4075. *Partial support by this grant*
16. J.D. Nicholas, L. Wang, A.V. Call and S.A. Barnett, "Use of the Simple Infiltrated Microstructure Polarization Loss Estimation (SIMPLE) model to describe the performance of nano-composite solid oxide fuel cell cathodes," *Phys Chem Chem Phys* 10.1039/c2cp43370b (2012). *Full support for Northwestern University effort by this grant.*
17. D.M. Bierschenk, J.M. Haag, K.R. Poeppelmeier and S.A. Barnett, "Performance and Stability of LaSr2Fe2CrO9- -Based Solid Oxide Fuel Cell Anodes in Hydrogen and Carbon Monoxide," *Journal of The Electrochemical Society* **160** (2012) F90-F93. *Partial support by this grant*
18. D.M. Bierschenk and S.A. Barnett, "Electrochemical characteristics of La0.8Sr0.2Cr0.82Ru0.18O3−δ–Gd0.1Ce0.9O2 solid oxide fuel cell anodes in H2–H2O–CO–CO2 fuel mixtures," *Journal of Power Sources* **201** (2012) 95-102. *Partial support by this grant*
19. S.A. Barnett, "Solid Oxide Fuel Cells: Direct Hydrocarbon Type," Encyclopedia of Electrochemistry / High-Temperature Electrochemistry, Springer, 2012. *Partial support by this grant*
20. T.C. Yeh, J.L. Routbort and T.O. Mason, "Oxygen transport and surface exchange properties of Sr0.5Sm0.5CoO3−δ," *Solid State Ionics* **232** (2013) 138-143 *Full Support From This Grant.*
21. Z. Zhan, D. Han, T. Wu, X. Ye, S. Wang, T. Wen, S. Cho and S.A. Barnett, "A Solid Oxide Cell Yielding High Power Density Below 600°C," *RSC Advances* (2012) Partial support by this grant.
22. J.M. Haag, D.M. Bierschenk, S.A. Barnett and K.R. Poeppelmeier, "Structural, Chemical, and Electrochemical Characteristics of LaSr2Fe2CrO9-Δ-Based Solid Oxide Fuel Cell Anodes," *Solid State Ionics* **212** (2012) 1-5 *Partial support by this grant.*
23. Z. Zhan, D.M. Bierschenk, J.S. Cronin and S.A. Barnett, "A Reduced Temperature Solid Oxide Fuel Cell with Nanostructured Anodes," *Energy & Environmental Science* (2011) *Partial support by this grant.*
24. Y. Liao, D.M. Bierschenk, S.A. Barnett and L.D. Marks, "Operational Inhomogeneities in La0.9Sr0.1Ga0.8Mg0.2O3-Δ Electrolytes and La0.8Sr0.2Cr0.82Ru0.18O3-Δ-Ce0.9Gd0.1O2-Δ Composite Anodes for Solid Oxide Fuel Cells," *Fuel Cells* **11** (2011) 635-641 *Full support by this grant.*
25. T. C. Yeh, N. H. Perry and T. O. Mason, "Nanograin Composite Model Studies of Nanocrystalline Gadolinia-Doped Ceria," J. Am. Ceram. Soc. 94 (2011) 1073-1078. *Full*

support by this grant.

26. N. H. Perry, T. C. Yeh and T. O. Mason, "Temperature Dependence of Effective Grain Core/Single Crystal Dielectric Constants for Acceptor-Doped Oxygen Ion Conductors," J. Am. Ceram. Soc. 94 (2011) 508-515. *Full support by this grant.*